RSC Advances

ROYAL SOCIETY OF CHEMISTRY

www.rsc.org/advances

Facile synthesis of CeO_2 decorated $Ni(OH)_2$ hierarchical composites for enhanced electrocatalytic sensing of H_2O_2

*Debao Wang[a], Limei Pang[b], Hongyu Mou[b], Yanhong Zhou[a], and Caixia Song[b]**

[a] State Key Lab Base of Eco-chemical Engineering, Lab of Inorganic synthetic and Applied Chemistry, Qingdao University of Science and Technology, Qingdao 266042, P. R. China

[b]College of Materials Science and Engineering, Qingdao University of Science and Technology, Qingdao 266042, P. R. China

* Corresponding author. E-mail: songcaixia@qust.edu.cn; Tel:86-532-84023653

Abstract CeO_2-$Ni(OH)_2$ composites with hierarchical structures were synthesized via a facile one-pot hydrothermal method, which were constructed with $Ni(OH)_2$ nanosheets decorated with in-situ formed CeO_2 nanoparticles on their surface. The composites were characterized by XRD, SEM, HRTEM, XPS, Raman spectroscopy, and electrochemical techniques. The results of nitrogen adsorption-desorption, electrochemical impedance spectroscopy, and amperometry demonstrated that CeO_2 and $Ni(OH)_2$ components of CeO_2-$Ni(OH)_2$ hierarchical architectures showed a synergistic contribution on the improvement of electrochemical activity toward H_2O_2. The oxidation current was linearly related to the H_2O_2 concentration from 0.5 μM to 1.2 mM. The sensor showed high sensitivity of 4.5 $\mu A \cdot \mu M^{-1} \cdot cm^{-2}$ with a lower detection limit of 0.035 μM (S/N=3). Moreover, the sensor showed good selectivity, reproducibility and stability. These results demonstrated the feasibility of the synthetic strategy and the potential of the composites as a promising candidate for H_2O_2 sensing.

1. Introduction

The development of efficient electrochemical H_2O_2 sensors has attracted tremendous research interests due to the significance of H_2O_2 in biological systems and

its practical applications.[1] Eenzyme-based H_2O_2 biosensors have been well-developed,[2–4] however, major limiting factors for their utility are the high costs of enzymes, complex electrode fabrication, and performance instability.[5] Recently, the development of nanomaterial-modified glassy carbon electrodes as nonenzymatic H_2O_2 sensors has attracted wide research interest, which is considered to have promising practical applications.[6] Various nanomaterials such as carbon nanotubes,[7] graphene,[8] transition metal oxides,[9,10] prussian blue,[11] noble metals,[12,13] and multi-component materials[14,15] have been employed as electrode materials to construct H_2O_2 sensors. Nevertheless, efficient utilization of nano-sized modifier usually suffers from undesirable conglomeration, where large surface areas and abundant active sites are lost and thus the performance is weakened. Accordingly, to develop a nonenzymatic H_2O_2 sensor with eco-friendly, high sensitivity and low cost are highly desirable to overcome the aforementioned limitations.

As a solution, significant efforts have been made to synthesize electrode materials with hierarchical morphology, which exhibits large surface area and more exposed active sites, and shows long-term stability performance.

Nickel hydroxide ($Ni(OH)_2$) is one of the most important transition metal hydroxides and has been widely investigated for its interesting electrochemical properties, which made $Ni(OH)_2$ as a promising material for applications in Ni-based alkaline secondary batteries,[16] electrochemical supercapacitors,[17,18] gas sensor,[19] and electrocatalysts.[20,21] The focus of recent researches has been on the potential of $Ni(OH)_2$ as electrochemical sensor materials.[22-27] For example, α-$Ni(OH)_2$ hierarchical architectures were synthesized and applied to electrochemical determination of H_2O_2.[28] Nanostructured CeO_2 has also attracted much attention for the development of electrochemical sensors and biosensors due to its good biocompatibility, vast surface-to-

bulk ratio, high chemical stability, and excellent electronic conductivity.[29,30] Ispas et al. reported the electrochemical studies of CeO_2 microspheres as an electrode material for sensing detection of H_2O_2.[29] Yagati et al. reported an enzymatic biosensor for H_2O_2 based on CeO_2 nanostructure films on indium tin oxide substrate.[31] Jha and co-workers constructed an electrochemical nonenzymatic H_2O_2 sensor based on CeO_2/reduced graphene oxide xerogel composite.[32]

On the basis of favorable electrochemical and electrocatalytic properties of $Ni(OH)_2$ and CeO_2 for detecting H_2O_2, herein, CeO_2 nanoplates were decorated on the surface of $Ni(OH)_2$ nanosheets which self-assemble in situ forming three-dimensional hierarchical structures through a facile one-pot hydrothermal method. The composites were modified onto a bare glassy carbon electrode to construct nonenzymatic H_2O_2 sensors. The structure evolution of the composites over time was investigated, and their structure-dependent sensing activities were evaluated. It is expected that the CeO_2–$Ni(OH)_2$ composites would exhibit a synergistic effect of both CeO_2 and $Ni(OH)_2$ components.

2 Experimental section

2.1 Synthesis of composite CeO_2-$Ni(OH)_2$ nanostructures

All of the chemicals were analytical-grade and were used without any further treatment. In a typical synthesis, 0.156 g $NiSO_4 \cdot 6H_2O$, 0.02 g $(NH_4)_2Ce(NO_3)_6$ and 0.1 g cetyltrimethylammonium bromide (CTAB) were dissolved in distilled water to form a homogeneous solution. Then, 0.2 g of hexamethylenetetramine (HMT) was added under vigorous stirring. The solution was transferred into a Teflon lined stainless steel autoclave and subsequently sealed. The autoclave was maintained at 180 °C for 6 h and then cooled to room temperature naturally. The green precipitates was separated from

the solution by centrifugation, washed with distilled water and absolute alcohol respectively, and then dried at 60 °C.

2.2 Characterization

The X-ray powder diffraction (XRD) patterns of the products were recorded on a D/max-2500/PC X-ray diffractometer with Cu Kα radiation (λ=1.5418 Å). The morphologies and microstructures of the products were characterized using a JSM-6700F field emission scanning electron microscope (SEM) and a JEM-2010 high-resolution transmission electron microscope (HRTEM). Nitrogen adsorption-desorption isotherms were obtained using a Micromeritics ASAP 2020 surface area analyzer to determine the Brunauer-Emmett-Teller (BET) surface area, Barrett-Joyner-Halenda (BJH) average pore size, and BJH cumulative volume of pores of the samples. Raman analysis was performed using a LabRam HR 800 laser confocal micro-Raman spectrometer (Jobin Yvon-Horiba) with a 532 nm YAG laser as the excitation source. X-ray photoelectron spectra were recorded on a Thermo ESCALAB 250XI multifunctional imaging electron spectrometer with Al Kα radiation (hν=1486.6 eV) at 150 W. The charging shifts of the spectra were calibrated using the C1s peak at 284.8 eV.

2.3 Electrode modification

Prior to the modification, a bare glassy carbon electrode (GCE) was carefully polished to a mirror-like surface using 0.3 μm alumina slurry and sonicated for at least 10 min in distilled water. Then the electrode was thoroughly rinsed with methanol and distilled water and subsequently dried at room temperature. 20 μL of CeO_2-$Ni(OH)_2$ nanostructure suspension (2.5 g/L) was dropped onto the surface of the polished GCE, then dried in air at room temperature for further use. The resulting electrodes were defined as CeO_2-$Ni(OH)_2$/GCE.

2.4 Electrochemical measurements

The electrochemical measurements were performed on a model CHI832B electrochemical analyzer (Shanghai CH Instrument Company, China) using a standard three-electrode cell. The modified electrode was used as a working electrode. A saturated Ag/AgCl electrode and a platinum wire were used as reference electrode and auxiliary electrode respectively. 0.1 mol/L KOH solution was used as the supporting electrolyte. Electrochemical behaviors of the electrodes toward H_2O_2 oxidation were characterized by cyclic voltammetry (CV) measurement at a scan rate of 50 $mV \cdot s^{-1}$. The amperometric curves were obtained with successive addition of a certain concentration of H_2O_2 with magnetic agitation under magnetic stirring. Electrochemical impedance spectroscopy (EIS) measurements were performed in 0.1 mol/L KCl containing 1.0 mmol/L $K_3[Fe(CN)_6]/K_4[Fe(CN)_6]$ at a bias potential of 0.172 V by applying an AC voltage with 5 mV amplitude in a frequency range from 10^{-2} Hz to 10^5 Hz under open circuit potential conditions and presented in Nyquist plots.

3. Results and discussion

3.1. Sample characterization.

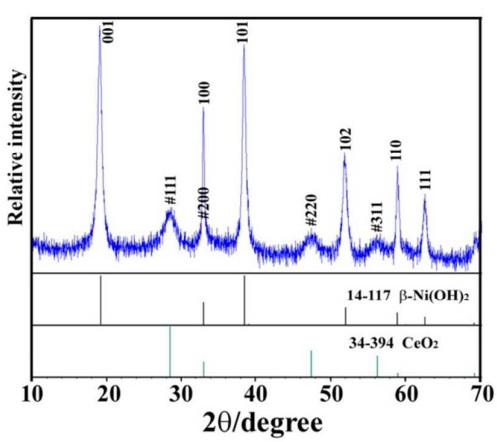

Fig. 1. XRD pattern of the CeO_2-$Ni(OH)_2$ Sample 2. The line pattern shows reference card according to JCPDS

The composition and phase purity of the as-synthesized product was identified by powder X-ray diffraction (XRD). As shown in Fig. 1, the sharp and strong diffraction peaks are labeled and can be indexed to β-phase hexagonal nickel hydroxide (JCPDS 14-117). The weak and broad diffraction peaks labeled with "#" can be attributed to cubic phase CeO_2 (JCPDS 34-394), which indicates that the product is CeO_2-$Ni(OH)_2$ composite. Comparing with the standard data, a slight decrease in 2θ values of β-$Ni(OH)_2$ peaks was recorded, and the lattice constants were calculated to be a = b = 0.3125 nm and c = 0.4638 nm for the sample. The *a* lattice constant is consistent with the standard value while the *c* lattice constant is larger than that of the β-$Ni(OH)_2$ unit cell (a= b = 0.3126 nm, and c = 0.4605 nm) , which indicates the increase of interlayer spacing of β-$Ni(OH)_2$ nanosheets and the possible doping of Ce atoms into the layered hexagonal crystal structure. Furthermore, an unusually high intensity of the (001) diffraction peak to (101) is observed, indicating the preferential crystal growth direction of the β-$Ni(OH)_2$ component.

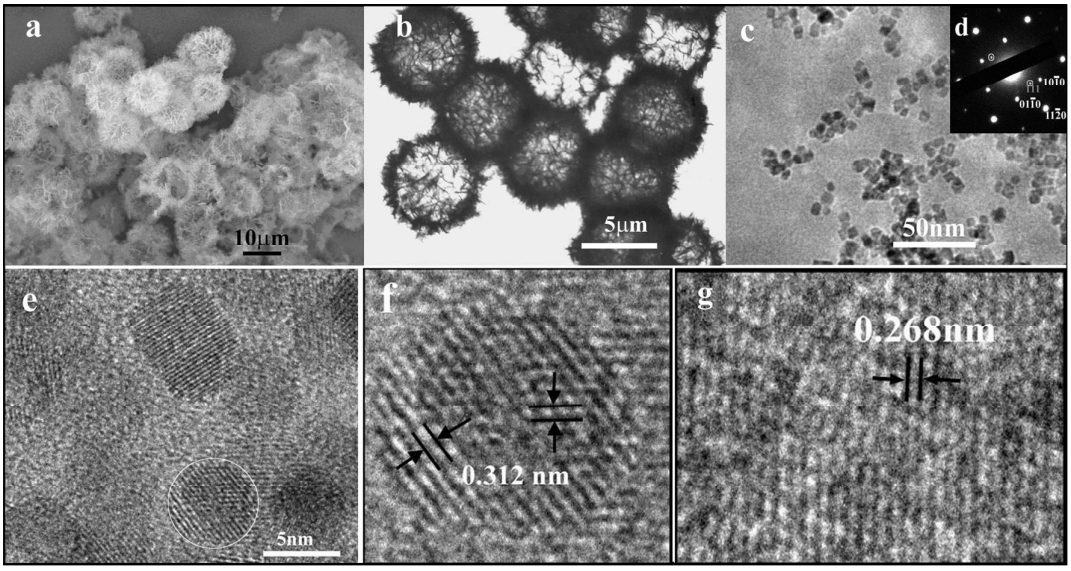

Fig. 2. (a) SEM and (b) TEM images of the CeO_2-$Ni(OH)_2$ sample 2. (c) TEM image, (d) ED pattern, and (e) HRTEM image of the composite nanosheets, and magnified HRTEM images of a CeO_2 nanoparticle (f) and the $Ni(OH)_2$ nanosheet (g).

SEM image in Fig. 2a shows that CeO_2-$Ni(OH)_2$ nanostructures are composed of symmetrical pompon-like microspheres with diameters of about 6.0 μm, which are built up with a lot of orderly attached nanosheets with thickness less than 10 nm. TEM image in Fig. 2b reveals that the pompon-like CeO_2-$Ni(OH)_2$ microspheres exhibit hollow structures. Fig. 2c shows TEM image of a nanosheet cracked from the microsphere by ultrasound irradiation. Obvious contrast can be observed between $Ni(OH)_2$ nanosheets and CeO_2 nanoparticles. $Ni(OH)_2$ nanosheets are composed of overlapped thinner layers. The well separated CeO_2 nanoparticles have a size ranging from 5 to 8 nm. The unique hierarchical structure of CeO_2-$Ni(OH)_2$ result from the hierarchical assembly of the $Ni(OH)_2$ nanosheets and the dispersed decoration of CeO_2 nanoparticles on their surfaces. The typical selected area electron diffraction (ED) pattern in Fig. 2d indicates the well crystallized nature of the nanosheets. The six symmetrical diffraction spots can be indexed to (10-10) and (01-10) planes of β-$Ni(OH)_2$ with a zone axis of [0001], while the spots marked with circles belong to (111) plane of cubic CeO_2. Fig. 2e clearly shows the HRTEM image of several CeO_2 nanoparticles. The enlarged image of the circled particle in Fig. 2f shows a d-spacing of 0.312 nm corresponding to (111) planes of the CeO_2 component. While the d-spacing of 0.268 nm in Fig. 2g corresponds to (100) planes of the β-$Ni(OH)_2$ component. It is evident some structure defects exist in both the components.

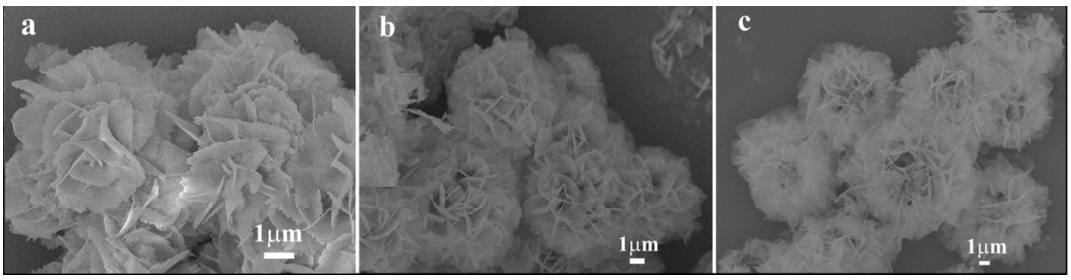

Fig. 3. SEM images of CeO_2-$Ni(OH)_2$ composites: (a) Sample 1, (b) Sample 3, and (c) Sample 4.

In order to investigate the morphology and microstructure evolution of the sample, the synthesis was conducted for different reaction time. Fig. 3 shows SEM images of the obtained CeO_2-$Ni(OH)_2$ composites. It can be seen from Fig. 3a that pompon-like structures have formed with loosely packed nanosheets after 3 h reaction. With the reaction time was prolonged to 12 h (Fig. 3b) or 24 h (Fig. 3c), the pompon-like structures grew more compact. Comparing with that shown in Fig. 2b, the nanosheets of the pompon grew thicker. Fig. S1 shows the SEM image of the bare $Ni(OH)_2$ sample prepared in the same condition. It can be seen that $Ni(OH)_2$ sample has similar pompon-like structures indicting that the decoration of CeO_2 nanoparticles has no obvious influence on the morphology of the product.

3.2 BET analysis.

To further reveal the inner architecture evolution of the CeO_2-$Ni(OH)_2$ composites, N_2 adsorption-desorption measurements were carried out to estimate the texture properties. Fig. 4 shows nitrogen adsorption-desorption isotherms and corresponding adsorption BJH pore size distribution curves of the CeO_2-$Ni(OH)_2$ samples. It can be seen that all samples exhibit type IV isotherms, indicating the presence of mesopores. Structure related properties were summarized in Table 1. It can be found that the BET specific surface area, BJH average pore diameter, and the corresponding total pore volume of the CeO_2-$Ni(OH)_2$ sample prepared for 6 h are much smaller than those of the sample prepared for 3 h, and slightly larger than those of the other two samples with longer reaction time. Sample 1 possesses much higher specific surface area, pore volume, and pore size, which may result from that, in the initial stage of the reaction (3h), freshly formed CeO_2-$Ni(OH)_2$ nanospecies have much lower crystallinity and much more structure defects as hinted in SEM image in Fig. 3a. When the reaction was prolonged to 6 h, well-crystallized hollow structures with porous structures were

obtained, which might benefit the electrocatalytic performance of the composites. When the hydrothermal reaction time was further prolonged to 12 h or 24 h, the crystallinity of CeO_2-$Ni(OH)_2$ composite would be further improved, the microstructures developed more compact and the nanosheets grew thicker as confirmed by SEM images in Fig. 3b and c. As a result, their specific surface area, pore volume, and average pore size become smaller, which may have influence on their electrocatalytic performance.

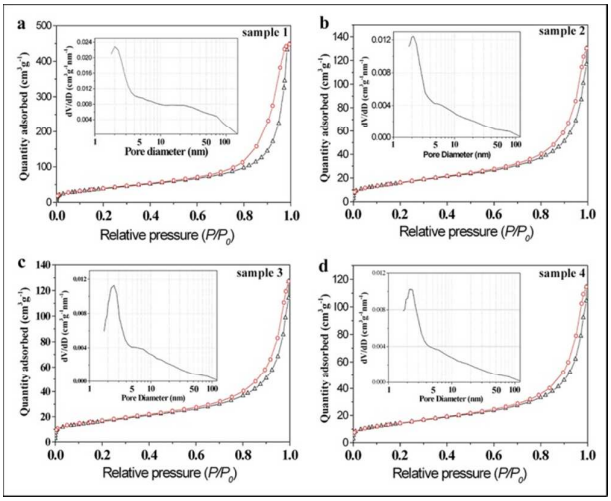

Fig. 4. N_2 adsorption-desorption isotherms and BJH-adsorption pore size distributions (insets) of the CeO_2-$Ni(OH)_2$ samples.

Table 1. Specific surface area, pore volume, and average pore size of the CeO_2-$Ni(OH)_2$ composites with different reaction time

Samples	Reaction time (h)	BET surface area（m^2g^{-1}）	Pore volume（m^3g^{-1}）	Adsorption average pore diameter（nm）
1	3	144.8	0.6888	17.27
2	6	59.14	0.1795	12.00
3	12	58.11	0.1776	11.78
4	24	54.96	0.1612	11.60

3.3 Raman analysis.

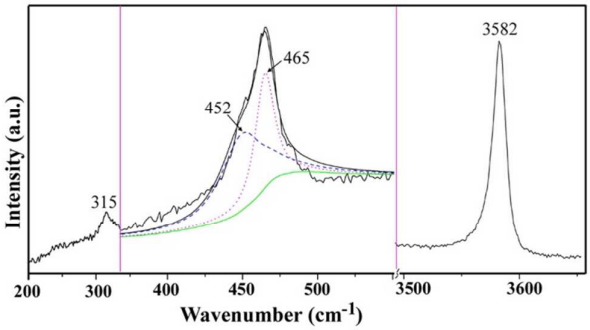

Fig. 5. Raman spectra of the CeO_2-$Ni(OH)_2$ sample 2.

To obtain further information on the microstructure of the as-prepared CeO_2-$Ni(OH)_2$, Raman spectroscopy is performed. The data presented in Fig. 5 show three characterized Raman shifts of β-$Ni(OH)_2$. The bands at 315, 452, and 3582 cm^{-1} can be assigned to an E-type vibration mode of the Ni–OH lattice, Ni-O stretching mode, and symmetric stretching mode of OH^-, respectively.[33,34] While the fitted signal at 465 cm^{-1} can be attributed to F2g mode vibration of the fluorite phase CeO_2.[35] Moreover, the Raman shifts exhibit broadening of the line and increases in asymmetry, indicating the formation of lattice defects or disorders in the as-obtained CeO_2-$Ni(OH)_2$ sample,[36,37] which is consistent with HRTEM results.

3.4 XPS analysis.

The surface composite and element valence states of the as-prepared CeO_2-$Ni(OH)_2$ sample were further determined by XPS analysis. Fig. 6a shows the O 1s electron core level XPS spectrum. One symmetric peak around 531.1 eV can be clearly seen, and it can be attributed to lattice oxygen ions in CeO_2-$Ni(OH)_2$. Since the position of Ce3d5/2 binding energy is superposed with the high binding energy side of Ni 2p1/2 signal, the peaks of Ce3d3/2 and Ni2p3/2 were used to detect the binding energy of Ni and Ce. Fig. 6b shows the XPS spectrum of Ni2p3/2. The main peak is located at 856.1 eV and is associated with a broad satellite at 861.0 eV. The binding energy of Ni^{2+} in the CeO_2-$Ni(OH)_2$ sample is slightly larger than the value reported for the pure β-$Ni(OH)_2$,[38]

which may indicate enhancement of the interaction between $Ni(OH)_2$ and CeO_2.[39] The core level Ce3d3/2 peaks are displayed in Fig. 6c. One can see that the XPS curve of Ce3d3/2 is somewhat rough, and this might be due to relatively low amount of CeO_2 nanoparticles decorated on the top surface of the composites.[40] As indicated by the fitted peaks, u, u', u'', u''' and u_0 come from Ce 3d3/2 state, v''' originates from Ce 3d5/2 states. The (u_0, u') states belong to Ce^{3+}, and (u, u'', u''') states correspond to Ce^{4+} oxidation state. This result indicates that both Ce^{4+} and Ce^{3+} ions coexist in CeO_2-$Ni(OH)_2$ sample. To keep charge neutrality in the presence of Ce^{3+} state in the sample, oxygen vacancies are formed, and the interface is the most preferential site for oxygen vacancies in oxide composites.[41-43] For CeO_2-$Ni(OH)_2$ sample, the stability of Ce^{3+} states and the concominant presence of oxygen vacancies is expected to favor the adsorption of H_2O_2 or O_2^{2-} species and electron transfer in CeO_2-$Ni(OH)_2$ sample.

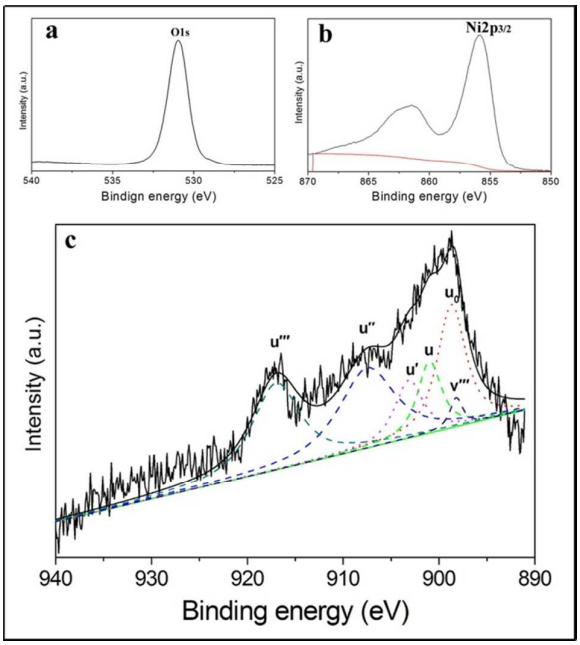

Fig. 6. XPS core level spectra of (a) O1s, (b) Ni2p3/2, and (c) Ce3d3/2 of the CeO_2-$Ni(OH)_2$ Sample 2.

3.5. Structure dependence of EIS and amperometric response.

It has been reported that EIS is an effective method for the understanding of chemical transformations and processes associated with a surface-modified electrode.[44] Generally, the curve of the EIS includes a semicircular part and a linear part. The linear part at lower frequencies corresponds to diffusion process and the semicircular part at higher frequencies represents the electron transfer limited process. The semicircle diameter corresponds to the electron-transfer resistance (R_{ct}). Fig. 7a shows the Nyquist plots of the EIS spectroscopies of different electrodes. An equivalent circuit for fitting the EIS results is presented in the inset of Fig. 7a, where R_s and R_{ct} correspond to solution resistance and charge transfer resistance, respectively. The parameter Z_w corresponds to the finite length Warburg impedance due to the mass diffusion and C_{dl} is the capacitance of the double layer. In EIS, the bare GCE exhibits an almost straight line, which implies the characteristic of a diffuse limiting step of the electrochemical processes. After CeO_2-$Ni(OH)_2$ composites being cast on the bare GCE, the semicircle diameters of EIS increase as compared to that of the bare GCE, which indicates that the composites have been modified onto the electrode surface. The characteristics of the EIS curves indicate that the electrode reaction occurring with CeO_2-$Ni(OH)_2$/GCE is controlled by charge transfer and proton diffusion. The impedance changes for different electrodes show that the nanostructure of CeO_2-$Ni(OH)_2$ can affect the electron transfer process. Clearly, the EIS is in the sequence with R_{ct} (sample 2) < R_{ct} (sample 3) < R_{ct} (sample 4) < R_{ct} (sample 1), which means that the electron transfer ability is in the order of R_{ct} (sample 2) > R_{ct} (sample 3) > R_{ct} (sample 4) > R_{ct} (sample 1). Comparing with the structure related properties of the four samples presented in Table 1, the variations of EIS were consistent with the differences of BET specific surface areas, BJH pore volumes, and average pore sizes for samples 2-4. But sample 1 is an exception. It may be probably attributed to its much larger surface area, BJH pore volume and average

pore size, which makes it possess much more open interface between the crystallites hindering the electron transfer on the modified electrode.

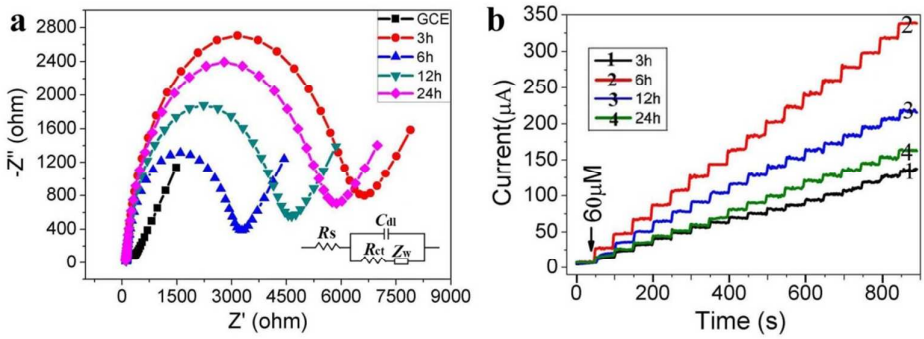

Fig. 7. (a) EIS and (b) Amperometric response of the electrodes modified with different CeO_2-$Ni(OH)_2$ samples. Inset of (a) is an equivalent circuit for the EIS results.

In order to further confirm the structure dependent electrochemical activities of the four CeO_2-$Ni(OH)_2$/GCE, their amperometric responses to H_2O_2 have been evaluated. The comparative amperometric response of different electrodes to successive addition of H_2O_2 is shown in Fig. 7b. For comparition, the amperometric response of the electrodes modified with bare $Ni(OH)_2$ and CeO_2-$Ni(OH)_2$ composites with different CeO_2 contents is shown in Fig. S2. It can be seen that all of the CeO_2-$Ni(OH)_2$/GCE and $Ni(OH)_2$/GCE have obvious electrocatalytic performance to H_2O_2. Moreover, CeO_2-$Ni(OH)_2$ composite obtained at 6 h exhibits the highest sensitivity under the test criterion, which might relate to their microstructures of the composite. And it made the CeO_2-$Ni(OH)_2$ sample 2 more suitable to construct a nonenzymatic electrochemical sensor toward the H_2O_2 detection. Structure dependence of amperometric response of the modified electrodes is similar to that of the EIS measurements. The enhancement of structure related electrocatalytic activity of CeO_2-$Ni(OH)_2$/GCE make CeO_2–$Ni(OH)_2$ composite a promising material for nonenzymatic sensing.

3.6. Electrochemical performance of the CeO_2-$Ni(OH)_2$/GCE

Based on the above results, the GCE was modified with CeO_2-$Ni(OH)_2$ sample 2, and its electrochemical performance as a H_2O_2 sensor was investigated by cyclic voltammetry in 0.1 M KOH solution. The modified electrode shows strong current responses and symmetric peak shape. The effect of scan rate on the electrochemical behavior of the CeO_2-$Ni(OH)_2$/GCE is presented in Fig. 8a. With increase in the scan rate from 2 to 100 $mV \cdot s^{-1}$, both the oxidation and reduction peak currents increase clearly accompanied with increased peak-to-peak separation. The plot of the peak currents versus the square root of the scan rate is shown in the inset of Fig. 8a. A good linear relation between the redox peak currents and the square root of the scan rate is obtained. It is well known that, in semi-infinite diffusion controlled cyclic voltammetry in liquid electrolytes, i (peak currents) against $\nu^{1/2}$ gives a linear relationship regardless of the scan rate for a kinetically uncomplicated redox reaction. While for an adsorption process, i against ν is expected to be linear at different scan rates. In the present study, the linear relationship between i and $\nu^{1/2}$ suggests that the observed electrochemical behavior of the CeO_2-$Ni(OH)_2$/GCE is a diffusion-controlled process, which is consistent with the $Ni(OH)_2$ nano(micro)-structures modified electrodes reported by other authors,[45-47] but is different from those reported for CeO_2 based biosensors, in which a surface-controlled process was observed.[31,48]

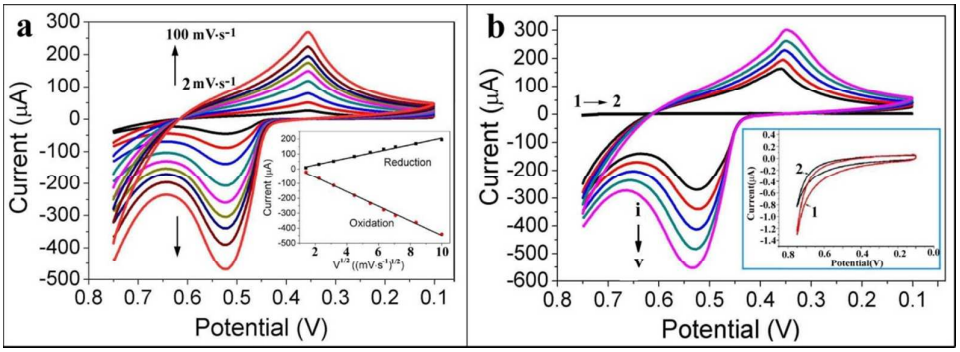

Fig. 8. (a) CVs of CeO_2-$Ni(OH)_2$/GCE with different scan rates (containing 60 μM H_2O_2). Inset of (a): peak currents versus square roots of scan rates. (b) CVs curves 1 and

2 for bare GCE in the absence and presence of 60 μM H_2O_2, and curves i to v for CeO_2-$Ni(OH)_2$/GCE in the presence of 0, 60, 120, 180, and 240 μM of H_2O_2, respectively. Inset of (b): enlarged image for curves 1 and 2.The scan rate was 50 $mV \cdot s^{-1}$.

In order to evaluate the electrocatalytic activity of the CeO_2-$Ni(OH)_2$/GCE as a nonenzymatic electrochemical sensor toward the H_2O_2 detection, typical CV curves were recorded at bare GCE and the CeO_2-$Ni(OH)_2$/GCE in 0.1 M KOH solution. Curves 1 and 2 in Fig. 8b and the inset relate to CV image of the bare GCE in the absence and presence of 60 μM H_2O_2 respectively. And no obvious response can be observed for bare GCE over the working potential range. However, for CeO_2-$Ni(OH)_2$/GCE, obvious response was recorded comparing with that of the bare GCE even in the absence of H_2O_2 (curve i). The peak current increases obviously after the same quantity H_2O_2 (60 μM) was added (curve ii). With increasing the concentration of H_2O_2 from 60 to 240 μM (curves ii to v), the redox peak currents gradually increase. As shown in Fig. 8b, the oxidation peak current is about 340 μA in the presence of 60 μM H_2O_2 (curve ii) and the peak current increases to 550 μA with increasing the concentration of H_2O_2 to 240 μM (curve v), which confirms that the modified electrode can be used as a sensor for quantitative analysis. The increase in both the oxidation and reduction peak currents with the addition of H_2O_2 is somewhat different from typical mediated electrocatalytic oxidation in which the reduction peak current is expected to decrease. It may relate to the fact that the transition between Ni(II) and Ni(III) makes this redox couple have a double function, the electronic medium as well as catalyst.[49] As well known, CeO_2 has been widely investigated as structural and electronic promoters to improve the activity, selectivity and thermal stability of catalysts.[50,51] And the CeO_2 component may also enhance the electron transfer rate and improve electrochemical behavior of the electrode

according to previous reports that CeO_2 component in a biosensor can provide electro-active surface and enhance electron transfer rate in the bioelectrode.[31,52] Comprehensively, from the above results, a proposed mechanism of the electrocatalytic oxidation of H_2O_2 via CeO_2-$Ni(OH)_2$/GCE is depicted in Fig. 9.

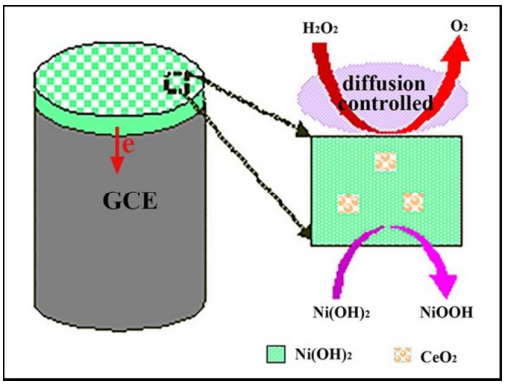

Fig. 9. Schematic mechanism for H_2O_2 detection based on CeO_2-$Ni(OH)_2$/GCE.

The higher activity of CeO_2-$Ni(OH)_2$ composite is not simply due to its smaller particle size or CeO_2/$Ni(OH)_2$ratio, but due to its unique hierarchical structure that enables effective supplying of H_2O_2 or O_2^{2-} species from CeO_2 to $Ni(OH)_2$ sites through intimate contact between the $Ni(OH)_2$ nanosheets and CeO_2 nanoparticles. In alkaline condition, the electrooxidation of H_2O_2 could be represented as follows:

$$Ni(OH)_2 + OH^- \rightarrow NiOOH + e^- + H_2O \quad (1)$$

$$H_2O_2 + 2OH^- \rightleftharpoons O_2^{2-} + 2H_2O \quad (2)$$

$$CeO_2 + O_2^{2-} \rightleftharpoons CeO_2(O_2^{2-})_{ads} \quad (3)$$

$$(O_2^{2-})_{ads} + 2\ NiOOH + 2H_2O \rightarrow O_2 + 2Ni(OH)_2 + 2OH^- \quad (4)$$

Due to the oxygen vacancies existing in CeO_2, H_2O_2 or O_2^{2-} species can be more easily adsorbed onto the electrode ($CeO_2(O_2^{2-})_{ads}$) and transfer to the surface of $Ni(OH)_2$ through spillover effect.[53] With charge transfer, H_2O_2 or O_2^{2-} species were oxidized into oxygen by NiOOH. It appears that the enhancement is likely to occur at the interface of

$Ni(OH)_2$ and CeO_2 in the composite. CeO_2-$Ni(OH)_2$ composite could combine the electrochemical characteristics of $Ni(OH)_2$ and the catalytic properties of CeO_2, which is helpful to improve the performance of the electrode.

3.7. Amperometric performance of the CeO_2-$Ni(OH)_2$/GCE sensor

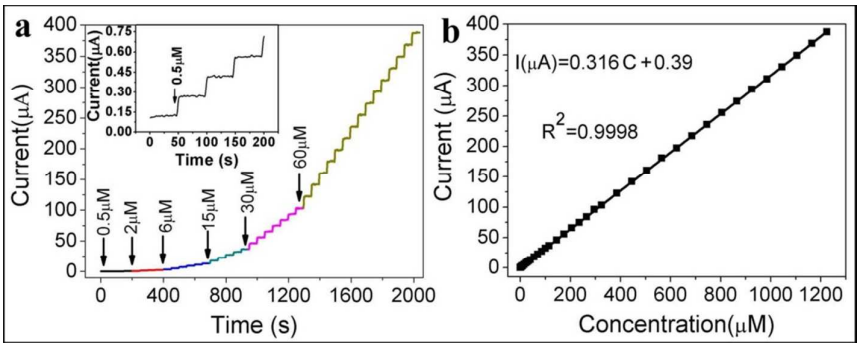

Fig. 10. (a) Typical amperometric response of CeO_2-$Ni(OH)_2$/GCE to successive addition of H_2O_2 at 0.52 V. (b) The plot of the response current versus H_2O_2 concentration. Inset of (a) shows the amperometric response to successive injection of 0.5 μM H_2O_2.

For amperometric sensing application, electrodes are usually evaluated by recording the current responses at a fixed potential with successive addition of the analyte. The performances of the CeO_2-$Ni(OH)_2$/GCE as a sensor for H_2O_2 was further evaluated using current–time responses. Fig. 10a shows the typical amperometric responses of CeO_2-$Ni(OH)_2$/GCE for the successive addition of H_2O_2 into a 0.1 M KOH solution with agitation at working potential of 0.52 V. The inset is the amplified response curve at the initial range displaying a stable and sensitive response for the determination of H_2O_2. Upon the addition of H_2O_2, the electrode can reach a steady-state response within 3 s with each injection of H_2O_2. The plot of the current as a function of H_2O_2 concentration is shown in Fig. 10b, which illustrates that the prepared CeO_2-$Ni(OH)_2$/GCE exhibits a good linear response to H_2O_2 concentrations in a range from 0.5 to 1200 μM with a sensitivity of 4.5 $\mu A \cdot \mu M^{-1} \cdot cm^{-2}$ and a detection limit of 0.035

μM (S/N=3). The regression equation, I (μA) = 0.316 *c* (μA/μM) + 0.39 (μA), has a correlation coefficient of 0.9998. These results were compared with those obtained for other electrodes modified with nanostructured materials. As listed in Table 2, it is clear that the sensor fabricated in this work had a wider linear range and a lower determination limit than the results reported for other H_2O_2 sensor which can be attributed to the direct electron transfer between CeO_2-$Ni(OH)_2$ and electrode without any immobilization matrix.

Table 2 Comparison of analytical performance of different H_2O_2 sensors

Electrode materials	Linear range	Detection	References
CeO_2-$Ni(OH)_2$	0.5 - 1200	0.035	This work
β-$Ni(OH)_2$ nanosheets/chitosan	5-145	0.5	(24)
β-$Ni(OH)_2$ nanoplates/Cu	5-145	1.5	(26)
α-$Ni(OH)_2$/FTO	5-1000	3.2	(27)
3D α-$Ni(OH)_2$/chitosan	1-216	…	(28)
β-$Ni(OH)_2$ nanoplates with (100) facet	0.1-10	…	(44)
$Ni(OH)_2$/SiNWs	?-5500	3.2	(54)
Ag nanowires/chitosan	8-1350	2	(55)
CeO_2/chitosan	2.2-320	0.098	(29)
HP/CeO_2/ITO biosensor	1-170	0.5	(48)
Au/CeO_2/chitosan biosensor	50-2500	7	(56)

3.8. Stability and selectivity of the Ce–$Ni(OH)_2$/GCE sensor

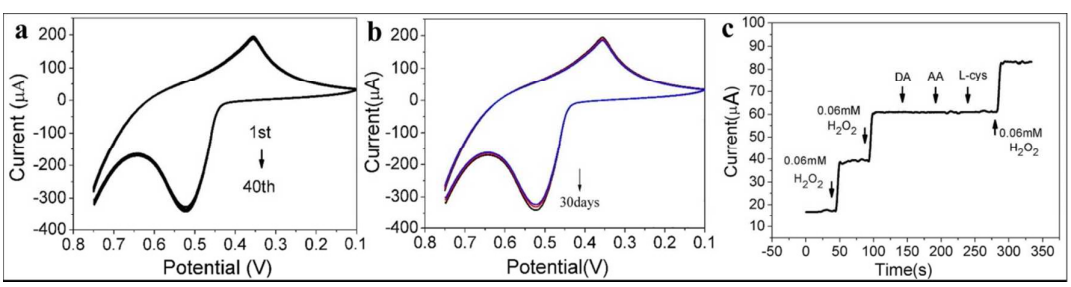

Fig. 11. CVs for the CeO_2-$Ni(OH)_2$/GCE with 60 μM H_2O_2: for 40 successive cycles (a), and being stored for different time (b). (c) Amperometric response for successive injection of 0.06 mM H_2O_2 and 0.6 mM interfering species (DA, AA, and l-Cys).

The CeO_2-$Ni(OH)_2$/GCE electrode exhibits a well-defined, stable, and sensitive response for the determination of H_2O_2. Fig. 11a shows the CV curves of the CeO_2-$Ni(OH)_2$/GCE measured in 0.1 M KOH solution containing 60 μM H_2O_2 with successive cycles under scan rate of 50 $mV \cdot s^{-1}$. The CV currents reached a steady state and maintained stable after the electrode was continuously scanned at the same conditions for 40 cycles. After being stored for 30 days at room temperature, the electrode still worked well (Fig. 11b), and the current responses toward 60 μM H_2O_2 maintained 98% of its initial responses. Based on the above results, it can be concluded that the prepared CeO_2-$Ni(OH)_2$/GCE shows good stability for H_2O_2 detection.

The selectivity of the CeO_2-$Ni(OH)_2$/GCE sensing H_2O_2 to different interfering agents was investigated at working potential 0.52 V. Dopamine hydrochloride (DA), l-ascorbic acid (AA), and L-Cysteine (L-Cys) were used as potential interfering agents towards the determination of H_2O_2. As shown in Fig. 11c, there is obvious current response with the addition of 0.06 mM H_2O_2. In contrast, no obvious current response is observed with the addition of 0.6 mM DA. The same instance is observed with the consecutive addition of 0.6 mM AA, and 0.6 mM L-Cys, which demonstrates that these substances do not show significant interference and the CeO_2-$Ni(OH)_2$/GCE has excellent selectivity to H_2O_2 determination.

The reproducibility of the CeO_2-$Ni(OH)_2$/GCE has also been investigated. Following the same procedure to modify the GCE, six CeO_2-$Ni(OH)_2$/GCE electrodes were fabricated with the same thickness, and were applied to the same H_2O_2 solution.

The relative standard deviation (RSD) value for H_2O_2 concentration was 3.5%. It indicates that the CeO_2-$Ni(OH)_2$/GCE has a good reproducibility and a high reliability.

4. Conclusion

In conclusion, three-dimensional CeO_2–$Ni(OH)_2$ composites with different microstructures were synthesized and were modified onto bare glassy carbon electrodes to construct an electrochemical H_2O_2 sensor. The structure-dependent sensing activity of the composites was evaluated by CV, amperometry, and EIS. The sensor exhibited excellent analytical performance to the detection of H_2O_2 with excellent selectivity, good stability and outstanding linearity from 0.5 μM to 1.2 mM with a detection limit of 0.035 μM (S/N=3). Our results demonstrated that the CeO_2-$Ni(OH)_2$/GCE is a promising choice for H_2O_2 detection and the CeO_2–$Ni(OH)_2$ nanocomposite is a promising material for nonenzymatic sensing, biosensing applications as well as other applications.

Acknowledgments This work is supported by National Natural Science Foundation of China (51272118, 51342005) and of Shandong Province (ZR2013BM002, ZR2011EMM007).

References

1 W. Chen, S. Cai, Q.Q. Ren, W. Wen, and Y.D. Zhao, Analyst, 2012, 137, 49-58.

2 M.-Y. Hua, Y.-C. Lin, R.-Y. Tsai, H.-C. Chen, and Y.-C. Liu, Microchim. Acta, 2011, 56, 9488−9495.

3 B.S. Munge, R.S. Dowd, C.E. Krause, and L.N. Millord, Electroanalysis, 2009, 21, 2241−2248.

4 K.-J Huang, D.-J. Niu, X. Liu, Z.-W. Wu, Y. Fan, Y.-F. Chang, and Y.-Y. Wu, Microchim. Acta, 2011, 56, 2947−2953.

5 F. Xu, M. Deng, G. Li, S. Chen, and L. Wang, Microchim. Acta, 2013, 88, 59−65.

6 J. Wang, Analyst, 2005, 130, 421-426.

7 Z.F. Li, J.H. Chen, W. Li, K. Chen, L.H. Nie, and S.Z. Yao, J. Electroanal. Chem., 2007, 603, 59-66.

8 L.Y. Cao, Y.L. Liu, B.H. Zhang, and L.H. Lu, ACS Appl. Mater. Interfaces, 2012, 2, 2339-2346.

9 Y.H. Lin, X.L. Cui, and L.Y. Li, Electrochem. Commun., 2005, 7, 166-172.

10 Y.-B. Hahn, R. Ahmad, and N. Tripathy, Chem. Commun., 2012, 48, 10369-10385.

11 C.X. Song, D.B. Wang, T. Yang, and Z.S. Hu, Sci. Adv. Mater., 2011, 3, 89-94.

12 Y.B. Zhou, G. Yu, F.F. Chang, B. Hu, and C.J. Zhong, Analy. Chim., Acta 2012, 757, 56-62.

13 K.Y. Zhang, N. Zhang, J.G. Xu, H.Y. Wang, C. Wang, H.W. Shi, and C. Liu, J. Appl. Electrochem., 2011, 41, 1419-1423.

14 K. Ye, D.M. Zhang, X.Wang, K. Cheng and D.X. Cao, RSC Advances, 2015, 5, 3239–3247.

15 D.M. Zhang, D.X. Cao, K. Ye, J.L. Yin, K. Cheng and G.L. Wang, Electrochim. Acta, 2014, 139, 250–255.

16 Z.L. Liu, S.W. Taya, and X. Li,, Chem. Commun., 2011, 47, 12473-12475.

17 H.Y. Sun, S.W. Liu, Q.F. Lu, and H.Y. Zhong, Mater. Lett., 2014, 128, 136-139.

18 Z.J. Luo, K. Wang, H.M. Li, S. Yin, Q.F. Guan, and L.G. Wang, CrystEngComm, 2011, 13, 7108–7113.

19 H.J. Wang, J. Gao, Z.G. Li, Y.L. Ge, K. Kan, and K.Y. Shi, CrystEngComm, 2012, 14, 6843–6852.

20 L.P. Xu, Y.S. Ding, C.H. Chen, L.L. Zhao, C. Rimkus, R. Joesten, and S.L. Suib, Chem. Mater., 2008, 20, 308-316.

21 J.W. Nai, Z.B. Chen, H.P. Li, F.Y. Li, Y. Bai, L.D. Li, and L. Guo, Chem. Eur. J., 2013, 19, 501-508.

22 M.A. Kiani, M.A. Tehrani, and H. Sayahi, Anal. Chim. Acta, 2014, 839, 26-33.

23 X.C. Song, X. Wang, Z.A. Yang, and Y.F. Zheng, Mater. Lett., 2011, 65, 2348-2350.

24 B. Fang, A.X. Gu, G.F. Wang, B. Li, C.H. Zhang, Y.Y. Fang, and X.J. Zhang, Microchim Acta, 2009, 167, 47-52.

25 G.X. Tong, F.T. Liu, W.H. Wu, J.P. Shen, X. Hu, and Y. Liang, CrystEngComm, 2012, 14, 5963-5973.

26 A.X. Gu, G.F. Wang, J. Gu, X.J. Zhang, and B. Fang, Electrochim. Acta, 2010, 55, 7182-7187.

27 P.R. Martins, A.G.N. Motta, M. Nakamura, K. Araki, and L. Angnes, Electroanalysis, 2013, 25, 2060–2066.

28 Z.C. Wu, C.R. Xu, H.M. Chen, H. Yu, Y.Q. Wu, and F. Gao, Mater. Res. Bull., 2013, 48, 2340-2346.

29 C. Ispas, J. Njagi, M. Cates, and S. Andreescu, J. Electrochem. Soc., 2008, 155, F169-176.

30 K.J. Feng, Y.H. Yang, Z.J. Wang, J.H. Jiang, G.L. Shen, and R.Q. Yu, Talanta, 2006, 70, 561-565.

31 A.K. Yagati, T. Lee, J. Min, and J.W.Choi, Biosens. Bioelectron., 2013, 47, 385-390.

32 S.K. Jha, C.N. Kumar, R.P. Raj, N.S. Jha, and S. Mohan,, Electrochimica Acta, 2014, 120, 308-313.

33 M.C. Bernard, R. Cortes, M. Keddam, H. Takenouti, P. Bernard, and S. Senyarich, J. Power Source, 1996, 63, 247-254.

34 B. Shruthi, V. Bheema Raju, and B.J. Madhu, Spectrochimica Acta Part A: 2015, 135, 683–689.

35 I. Kosacki, T. Suzuki, H.U. Anderson, and P. Colomban, Solid State Ionics, 2002, 149, 99–105.

36 H. Li, A. Petz, H. Yan, J.C. Nie, and S. Kunsági-Máté, J. Phys. Chem. C, 2011, 115, 1480–1483.

37 W.H. Weber, K.C. Hass, and J.R. McBride, Phys. Rev. B, 1993, 48, 178-185.

38 Z.P. Yan, X.X. Yu, Y.Y. Zhang, H.X. Jia, Z.J. Sun, and P.W. Du, Applied Catalysis B, 2014, 160–161, 173–178.

39 L. Pastor-Pérez, and R. Buitrago-Sierra, A. Sepúlveda-Escribano, Int. J. Hydrogen Energy, 2014, 39, 17589–17599.

40 M.A. Scibioh, S.K. Kim, E.A. Cho, T.H. Lim, S.A. Hong, and H.Y. Ha, *Appl. Catal. B: Environ.* 2008, *84*, 773–782.

41 M.J. Muñoz-Batista, M.N. Gómez-Cerezo, A. Kubacka, D. Tudela, and M. Fernández-García, ACS Catal., 2014, 4, 63−72.

42 A.C. Johnston-Peck, S.D. Senanayake, J.J. Plata, S. Kundu, W. Xu, L. Barrio, J. Graciani, J.F. Sanz, R.M. Navarro, J.L.G. Fierro, E.A. Stach, and J.A. Rodriguez, J. Phys. Chem. C, 2013, 117, 14463−14471.

43 P. Trogadas, J. Parrondo, and V. Ramani, ACS Appl. Mater. Interfaces, 2012, 4, 5098−5102

44 X.J. Zhang, A.X. Gu, G.F. Wang, B. Fang, Q.Y. Yan, J.X. Zhu, T. Sun, J. Ma, and H.H. Hng, CrystEngComm, 2011, 13, 188-192.

45 X.H. Yue, J.Q. Pan, Y.Z. Sun, and Z.H. Wang, Ind. Eng. Chem. Res., 2012, 51, 8358-8365.

46 H.B. Zhou, and Z.T. Zhou, Chin. J. Chem., 2006, 24, 37-44.

47 M.A. Kiani,; M.F. Mousavi, and S. Ghasemi, J. Power Sources, 2010, 195, 5794-5800.

48 A.A. Ansari, P.R. Solanki, and B.D. Malhotra, J. Biotechnol., 2009, 142, 179-184.

49 C.Z. Zhao, S. Shao, M. Li, and K. Jiao, Talanta, 2007, 71, 1769-1779.

50 T. Brezesinski, J. Wang, R. Senter, K. Brezesinski, B. Dunn, and S. H. Tolbert, ACS nano, 2010, 4(2), 967–977.

51 Z. Tang and G. Lu, Appl. Catal. B: Environ. 2008, 79, 1-7

52 A.A. Ansari, A. Kaushik, P.R. Solanki, and B.D. Malhotra, Electrochem. Commun., 2008, 10, 1246-1249.

53 C. Li, Y.Z. Song, Y.X. Chen, X.W. Han, Q. Xin, and W.Z. Li, Studies in Surf. Sci. & Catal., 1997, 112, 439

54 Q. Yan, Z.L. Wang, J. Zhang, H. Peng, X.J. Chen, H.N. Hou, and C.R. Liu, Electrochim. Acta 2012, 61, 148-153.

55 X. Gao, L.Y. Jin, Q. Wu, Z.C. Chen, and X.F. Lin, Electroanalysis, 2012, 24, 1771-1777.

56 W. Zhang, G.M. Xie, S.F. Li, L.S. Lu, and B. Liu, Appl. Surf. Sci., 2012, 258, 8222-8227.